Polyurethane-polyurea hybrid nanocapsules as efficient delivery systems of anticancer Ir(III) metallodrugs

Joaquín Bonelli,[1,2,#] Enrique Ortega-Forte,[3,#] Gloria Vigueras,[3,#] Manel Bosch,[4] Natalia Cutillas,[3] Josep Rocas,[2] José Ruiz,[3,*] Vicente Marchán[1,*]

[1] Departament de Química Inorgànica i Orgànica, Secció de Química Orgànica, IBUB, Universitat de Barcelona, E-08028 Barcelona, Spain. Email: vmarchan@ub.edu

[2] Nanobiotechnological Polymers Division, Ecopol Tech, S.L., El Foix Business Park, Indústria 7, 43720 L'Arboç del Penedès, Tarragona, Spain

[3] Departamento de Química Inorgánica, Universidad de Murcia, and Institute for Bio-Health Research of Murcia (IMIB-Arrixaca), E-30071 Murcia, Spain. Email: jruiz@um.es

[4] Unitat de Microscòpia Òptica Avançada, Centres Científics i Tecnològics, Universitat de Barcelona, Av. Diagonal 643, E- 08028 Barcelona (Spain)

# These authors contributed equally

ABSTRACT

Cyclometalated Ir(III) complexes hold great promise as an alternative to platinum metallodrugs for therapy and diagnosis of cancer. However, low aqueous solubility and poor cell membrane permeability difficult *in vivo* applications. Here we have encapsulated for the first time, using polyurethane-polyurea hybrid nanocapsules (NCs), two phosphorescent tris-cyclometalated Ir(III) complexes incorporating deprotonated 2-arylbenzimidazole ligands, **Ir1** and **Ir2**. Ir(III)-loaded nanocapsules (**NC-Ir1** and **NC-Ir2**) showed a roughly round shape and controlled particle size distribution around 18 nm. The photophysical properties of aqueous solutions of NCs were similar to those of the free complexes in CH_2Cl_2, which accounts for the hydrophobic and protective environment generated by the nanoparticles around the cargo. Nanoencapsulation had also a positive effect on the cellular uptake of the metallodrugs and NCs were found highly cytotoxic towards several cancer cell lines, whereas Ir(III) complexes alone were found inactive. A strong tumor growth inhibition effect was also found in 3D tumorsphere cancer models owing to the high penetration capacity of small NCs. Finally, the mode of cell death of the NCs was found to be related with oncosis, and mitochondrial dysfunction and generation of extensive oxidative stress appeared to be also involved in the mechanism of action of these novel nanomedicines.

GRAPHICAL ABSTRACT
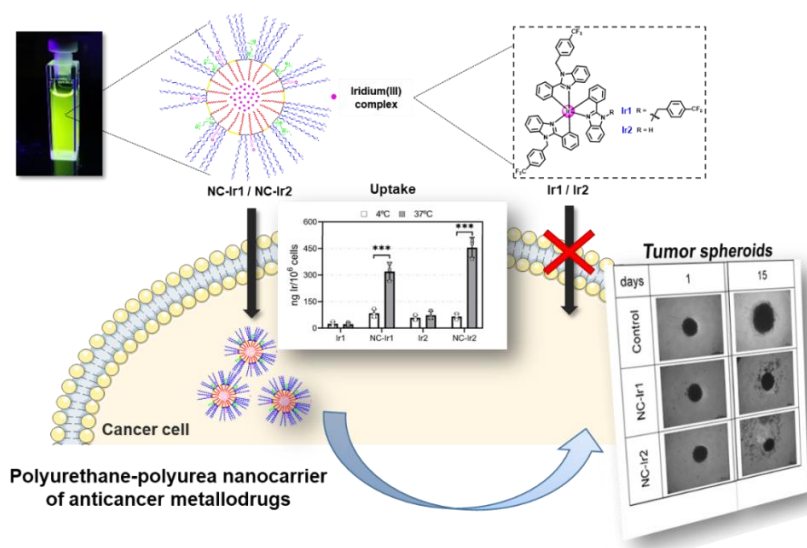
KEYWORDS

Nanoparticles, Nanoencapsulation, Iridium metallodrugs, Drug delivery, Antitumor agents

1. INTRODUCTION

Metal complexes have shown impressive properties in different medical fields, especially in oncology, where platinum(II)-based drugs such as cisplatin and its second and third generation analogues are prescribed in most of the first line anticancer treatments in the clinics.[1] Nevertheless, these compounds exhibit several serious drawbacks, including systemic toxicity in patients due to poor tumor specificity, and premature degradation/inactivation in blood stream, which become crucial issues to be considered when developing a safely metallodrug-based antitumor therapy.[2] Hence, controlled accumulation and release of metal-based anticancer drugs have aroused enormous interest in the last decades with the aim of improving their therapeutic efficacy.[3] In this context, nanosystems have been postulated as efficient carriers for enhancing metallodrugs' concentration in tumor cells.[3-4] Indeed, most of the common nanomedical approaches, such as metal-organic frameworks (MOF),[5] liposomes,[6] micelles[7] or polymeric nanoparticles[8] and nanocapsules,[9] have been explored as potential candidates for targeted delivery of metallodrugs. In the case of liposoluble compounds, the effect of the nanocarrier should not only be restricted to enhance their accumulation in target tissues, but also to improve selective internalization in cancer cells, which really triggers their cytotoxic effect.

Polyurethanes have gained interest in different biomedical applications, from stents[10] or catheter implants[11] to "polymeric director" groups[12] and nanocapsules,[13] since they exhibit reasonable toxicity and biocompatibility, together with accessible and feasible synthetic procedures. Polyurethane-polyurea hybrid nanocapsules (NCs) have been previously reported by our group as promising tools for different nanomedical solutions,[14] for example, in the fields of immunotherapy[15] and regenerative medicine.[16] This approach takes advantage of the versatility provided by polyurethane chemistry to furnish water-dispersible, with no external surfactants needed, and industrial-scalable drug-loaded nanocapsules.[17] In addition, the combination of amphiphilic groups and the ability of modifying their external surface charge under extracellular tumor microenvironment (TME) conditions, increasing their positive surface charge in acidic media, results in a higher accumulation in tumor locations compared with healthy tissues, and increased uptake by tumor cells.[17]

On the other hand, the use of Ir(III) complexes in therapy as an alternative to platinum metallodrugs has increased in the last years.[18] This is mainly because Ir(III) compounds possess several advantages with respect platinum complexes such as easier preparation and purification, air and moisture stability and remarkable tunability of their photophysical

properties. In addition, the combination of both anticancer activity and luminescence in octahedral cyclometalated Ir(III) complexes has allowed the development of new theranostic agents which offer both therapeutic promise and potential for diagnosis.[19] Hitherto, neutral Ir(III) complexes have been the most studied phosphorescent materials[20] since they exhibit excellent properties, including stability of the octahedral geometry in both reduced and oxidized states and long emission lifetimes, high quantum yields and tunable emission color.[20a] However, highly luminescent tris-cyclometalated iridium(III) complexes have been used to a much smaller extent in living systems than cationic bis-cyclometalated compounds. One of the reasons may be that they are generally electronic-neutral molecules and thus have very low water solubility. Therefore, the structures of complexes have been modified with cationic peptides,[21] groups that increase water solubility,[22] or groups that are pH sensitive.[23] Another strategy consists of using nanocarriers that transport the complexes inside the cells.[24] Thus, Ir(III) complexes incorporated in nanometric drug delivery systems could improve their biological performance, especially in terms of cellular uptake, solubility and biocompatibility.[25]

Herein, we present the encapsulation, using polyurethane-polyurea hybrid nanocapsules, of two new phosphorescent, hydrophobic and neutral homo- or hetero- tris-cyclometalated Ir(III) complexes of the type $[Ir(C^{\wedge}N)_3]$ (**Ir1**) and $[Ir(C^{\wedge}N)_2(C'^{\wedge}N')]$ (**Ir2**) (Figure 1), with the aim of exploring their photophysical, cellular uptake and biological properties. The C^N ligands in both complexes have in common the benzimidazole core which has been shown to be a widely used pharmacophore[26] and has exhibited good biological performance in previous works of some of us.[27] The Ir(III)-loaded nanocapsules were efficiently internalized in living HeLa cells compared to free complexes, and their photophysical properties resembled to those of the compounds dissolved in an organic solvent owing to the hydrophobic and protective environment provided by the nanocapsules around the compounds. Besides studying the antiproliferative activity of the Ir(III)-loaded NCs in 2D monolayer cancer cells and in 3D tumorsphere cancer models, the mode of cell death was investigated in detail.
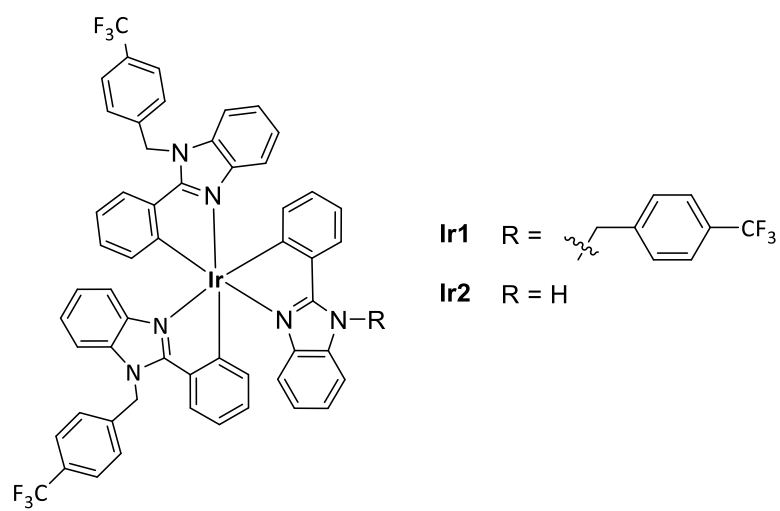
Figure 1. Structure of tris-cyclometalated Ir(III) complexes, **Ir1** and **Ir2**, investigated in this work.

2. EXPERIMENTAL SECTION

2.1. Synthesis and characterization of Ir(III) complexes

The first step for both complexes was the synthesis of the dimer complex $[(Ir(\mu\text{-}Cl)(C^\wedge N)_2]_2$, which was carried out following a previously reported procedure.[28] 2-Phenyl-1-[4-(trifluoromethyl)benzyl]-1H-benzo[d]imidazole (2.2 mmol) and iridium(III) chloride (1 mmol) were dissolved in 2-ethoxyethanol/deionized H_2O (3:1) in a Schlenk flask. The mixture was stirred at 110 ºC for 24 h under a nitrogen atmosphere. The mixture was cooled to room temperature, and the resultant solid was collected by filtration. The yellow solid was washed with water and ethanol and used without further purification.

2.1.1. Synthesis and characterization of Ir1

The homoleptic complex **Ir1** was synthesized using an adaptation of a previously reported method.[29] A solution of the cyclometalated iridium(III) chloro-bridged dimer (0.081 mmol), 2-phenyl-1-[4-(trifluoromethyl)benzyl]-1H-benzo[d]imidazol (0.59 mmol), and silver triflate (0.16 mmol) in 2-ethoxyethanol (2 mL) was heated at 95 °C overnight under nitrogen atmosphere. The solvent was concentrated under reduced pressure, and the product was re-suspended in dichloromethane. The suspension was filtered with celite to remove the white AgCl precipitate, and the filtrate was solvent-stripped to dryness. Then, the obtained solid was washed with ethyl acetate to obtain the bright yellow product.

Ir1. Bright yellow solid. Isolated yield: 65%. ^{1}H-NMR (300 MHz, [D$_2$]Methylene Chloride): δ (ppm) 7.55 (d, J= 8.1 Hz, 2H), 7.46 (m, 1H), 7.29 (m, 4H), 6.87 (t, J= 7.2 Hz, 1H), 6.72 (m, 3H), 6.50 (d, J= 8.1 Hz, 1H), 5.97 (m, 2H). ^{13}C-NMR (75.4 MHz, [D$_2$] Methylene Chloride): δ (ppm) 163.7, 142.9, 141.0, 138.4, 136.9, 135.8, 131.1, 130.7, 130.1, 127.4, 127.0, 127.0, 125.3, 124.3, 123.8, 120.7, 117.1, 110.8, 48.8. ESI-MS (pos. ion mode, CH_2Cl_2): m/z = 1247.3001 [M+H]$^+$, calcd. m/z 1247.3035. Anal. Calcd. for $C_{63}H_{42}F_{12}IrN_6$: C, 60.72; H, 3.40; N, 6.74. Found: C, 60.66; H, 3.41; N, 6.62 (%).

2.1.2. Synthesis and characterization of Ir2

The heteroleptic complex **Ir2** was synthesized using an adaptation of a previously reported method.[30] The iridium(III) dimer (1 mmol), 2-phenyl-1H-benzo [d]imidazole (10 mmol), and Na_2CO_3 (2 mmol) were all suspended in 2 mL of 2-ethoxyethanol. The mixture was refluxed for 3 h and the solid was filtered after cooling in the fridge for 2 hours. The crude was purified by chromatography column on silica gel eluting with dichloromethane.

Ir2. Yellow solid. Isolated yield: 31%. ^{1}H-NMR (300 MHz, [D$_2$]Methylene Chloride): δ (ppm) 9.65 (s, 1H), 7.50 (m,7H), 7.29 (m, 5H), 7.17 (m, 3H), 6.83 (m, 4H), 6.71 (m, 6H), 6.46 (d, *J*=7.8 Hz, 1H), 6.40 (d, *J*=8.4 Hz, 1H), 6.32 (d, *J*=7.5 Hz, 1H), 6.07 (s br, 1H), 6.01 (s br, 1H), 5.93 (d, *J*=5.8 Hz, 1H), 5.71 (d, *J*=6.2 Hz, 1H). ^{13}C-NMR (75.4 MHz, [D$_2$]Methylene Chloride): δ (ppm) 174.5, 164.1, 163.2, 163.7, 143.5, 142.9, 142.8, 141.0, 138.5, 138.3, 137.8, 136.8, 135.7, 135.5, 134.1, 134.0, 131.1, 130.7, 130.5, 127.4, 127.0, 126.9, 125.4, 125.3, 124.5, 124.3, 123.9, 123.7, 123.7, 120.5, 120.4, 120.3, 117.1, 116.6, 112.6, 110.7, 110.6, 48.8. HR ESI-MS (pos ion mode, DMSO): *m/z* = 1089.2669 [M+H]$^+$, calcd. *m/z* 1089.2691. Anal. Calcd. for C$_{55}$H$_{37}$F$_6$IrN$_6$. C, 60.71; H, 3.43; N, 7.72. Found: C, 60.82; H, 3.43; N, 7.60 (%).

2.2. Synthesis of Ir(III)-loaded nanocapsules

2.2.1. Synthesis of amphiphilic cationic polymer (P1)

2,2´-Dihydroxyethyl disulfide (DEDS) (901.0 mg, 5.84 mmol, 11.68 meq), YMER N120 (12.04 g, 11.59 mmol, 23.18 meq) and *N*-(3-dimethylaminopropyl)-*N,N*´-diisopropanolamine (Jeffcat DPA) (981.3 mg, 4.50 mmol, 8.99 meq) were added into a three-necked round-bottom flask equipped with mechanical stirring at room temperature and purged with N$_2$. When the mixture was homogeneous, isophorone diisocyanate (IPDI) (8.14 g, 36.63 mmol, 73.24 meq) was added into the reaction vessel under gentle mechanical stirring. The polyaddition reaction was kept under these conditions until the NCO stretching band intensity did not change, monitored by IR spectroscopy. At this point, dry THF (21 mL) was added into the reaction mixture in order to fluidify the polymer. In parallel, 1,3-diamino-*N*-octadecylpropane (Genamin TAP 100D) (5.99 g, 17.73 mmol, 35.45 meq) was dissolved with dry THF (5.23 mL) into another 100 mL three-necked round-bottom flask, which had previously been purged with N$_2$. The former reaction mixture was added dropwise onto the latter under half-moon 100 rpm mechanical stirring. The reaction was monitored by IR until the NCO stretching band intensity had completely disappeared.

2.2.2. Synthesis of Ir1-loaded amphoteric NCs (NC-Ir1)

IPDI (70.1 mg, 0.32 mmol, 0.63 meq) was added into a three-necked round-bottom flask equipped with mechanical stirring, precooled at 4 °C, purged with N$_2$ and protected from light. In parallel, **Ir1** (6.1 mg, 4.89 μmol), Neobee 1053 (26.0 mg, 55.96 ☐mol), polymer P1 (813.7 mg, 0.09 meq) and dry THF (1 mL) were mixed in a vial, added into the flask and homogenized for 10 min at 150 rpm, protected from light. At this point, an alkaline aqueous solution of L-lysine was prepared by dissolving 0.93 g of L-lysine in 12.31 g of Milli-Q water and adjusting pH to 11.0 with 3 M and 1 M NaOH solutions (total L-lysine concentration

7.56% by wt). This solution (24.6 mg of L-lysine, 0.15 mmol, 0.29 meq) was added at 250 rpm and the polyaddition reaction was checked after 15 min by IR. Then, the organic phase was emulsified at 300 rpm with cold Milli-Q water (7.12 g) and finally a 10% w/w aqueous solution of diethylenetriamine (DETA) (7.94 mg of DETA, 0.08 mmol, 0.23 meq) was added in order to generate crosslinked NCs from the nano micelles. The stirring was reduced to 100 rpm. This polyaddition reaction was monitored by IR and pH measurements. Once the NCs were formed, THF was removed from the reactor at 35 °C under vacuum and the dialysis purification was carried out.

2.2.3. Synthesis of Ir2-loaded amphoteric NCs (NC-Ir2)

Encapsulation of complex **Ir2** was carried out following the procedure used for the synthesis of **Ir1**-loaded amphoteric NCs. The exact amounts of the reagents used are detailed in Table S1.

2.2.4. Synthesis of non-loaded amphoteric NCs (NC-GTCC)

The procedure was based on the one used for the synthesis of **Ir1**-loaded amphoteric NCs with the exception that no iridium complex was added to the reaction. The exact amounts of the reagents are detailed in Table S2.

2.3. Biological studies

2.3.1. Cell culture

HeLa cervical cancer cells and BGM primate kidney cells were cultured in Dulbecco's Modified Eagle Medium (1 g/L glucose) and supplemented with fetal bovine serum (10% v/v) and 1 mM L-glutamine in a CO_2 incubator at 310 K. Sensitive and resistant A2780 and A2780cis ovarian cancer cells were cultured in RPMI-1640 cell media, supplemented with 10% fetal bovine serum and 1 mM L-glutamine. Cell culture was maintained with a subculture routine of 2–3 times a week with an appropriate density for each cell line. To maintain the resistance to cisplatin of A2780cis, cisplatin (1 μM) was added to culture media every second passage. Cells were confirmed to be mycoplasma-free using a standard Hoechst staining method.[31]

For cell treatments, both compounds and nanoparticles were prepared in serial dilutions using eppendorf tubes. For compounds **Ir1** and **Ir2**, serial dilutions with sterile DMSO as a solvent were prepared to obtain stock solutions that were 250X concentrated. Then, cell media was used to further dilute the samples until 10X. By dispensing 10% of the volume per well into the cell plates, a final 1X concentration was achieved with final 0.4% DMSO (v/v). For

nanoparticles **NC-Ir1** and **NC-Ir2**, stock water-dissolved solutions were directly diluted in cell media and were used for treatments thereafter.

2.3.2. Cellular accumulation by ICP-MS

Cellular accumulation from iridium complexes (**Ir1** and **Ir2**) and from iridium-containing nanocapsules (**NC-Ir1** and **NC-Ir2**) was measured in HeLa cells. The cells were seeded in 6-well plates at a density of $6 \cdot 10^5$ cells/well in 1.8 mL of complete growth medium and incubated for 48 h prior treatment. Cells were then treated with 5 μM of the iridium complexes or nanocapsules for 2 h at 37 ℃ and 4 ℃. After trypsinization, cells were counted and the pellets digested using Suprapur® nitric acid 30 % for 1 h. The amount of iridium was determined using Inductively Coupled Plasma Mass Spectrometry (ICP-MS). Three independent measurements were conducted (n=2 replicate).

2.3.3. Cellular uptake by confocal microscopy

HeLa cells were maintained in DMEM (Dullbecco Modified Eagle Medium) Corning Glutagro™ (10-101-CV) containing high glucose (4.5 g/L) and supplemented with 10% FBS (Fetal Bovine Serum (FBS) and 50U/mL penicillin-streptomycin. For cellular uptake experiments and posterior observation under the microscope, cells were seeded on glass bottom dishes (P35G-1.5-14-C, Mattek). 24 h after cell seeding, cells were incubated at 37 ℃ for 30 min with free (**Ir1** and **Ir2**) and encapsulated iridium compounds (**NC-Ir1** and **NC-Ir2**) (5 μM) in supplemented DMEM. Then, cells were washed three times with DPBS (Dulbecco's Phosphate-Buffered Saline) to remove the excess of the compounds and kept in low glucose (1 g/L) DMEM without phenol red for fluorescence imaging.

All microscopy observations were performed using a Zeiss LSM 880 confocal microscope equipped with 405 and 488 nm lasers. The microscope was also equipped with a full enclosure imaging chamber (XLmulti S1, Pecon) connected to a 37 ℃ heater and a 5% CO_2 providing system. Cells were observed using a 63X 1.4 oil immersion objective. The Ir(III) complexes were excited using the 405 nm laser and detected from 423 to 547 nm whereas iridium-containing nanocapsules were excited at 488 nm and detected from 497 to 597 nm. Image analysis was performed using Fiji.[32] Unless otherwise stated images are colorized using Fire lookup table.

2.3.4. Antiproliferative activity.

A2780, A2780cis and HeLa cells were cultured in 96-well plates at a density of 5000 cells/well in complete medium and incubated for 24 h in a humidified CO_2 incubator at 37 ℃.

Serial dilutions of NC particles were added at final concentrations in the range of 0 to 30 mg/mL in a final volume of 100 μL per well for indicated periods of time. After this incubation period, treatment-containing medium was aspirated by suction, cells washed with saline PBS buffer and loaded with 50 μL of MTT solution (1 mg/mL) for additional 4 h, then removed and 50 μL DMSO was added to solubilize the purple formazan crystals formed in active cells. The absorbance was measured at 570 nm using a microplate reader (FLUOstar Omega) and the IC_{50} values were calculated based on the inhibitory rate curves using the next the equation:

$$I = \frac{I_{max}}{1 + \left(\frac{IC_{50}}{C}\right)^n}$$

Where I represent the percentage inhibition of viability observed, I_{max} is the maximal inhibitory effect, IC_{50} is the concentration that inhibits 50% of maximal growth, C is the concentration of the treatment and n is the slope of the semi-logarithmic dose-response sigmoidal curves. The non-linear fitting was performed using SigmaPlot 14.0 software. All experiments were performed in at least two independent studies with triplicate points per concentration level (n=3).

For generation of multicellular tumor spheroids (MTCS), 96-well Corning® microplates with Ultra-Low Attachment surface coating were used. Briefly, a single suspension of HeLa cells at a density of $5\cdot10^3$ cells/well was prepared in complete DMEM medium and dispensed into wells. The plates were covered and transferred to incubator at 37 °C with 5% CO_2 atmosphere. Within 3-4 days, uniform 200 μm-diameter MTCS were formed from cell suspension and were maintained under these conditions. Cell culture medium was replaced every 3 days and treated **NC-Ir1** and **NC-Ir2** (6 μM) by replacing 50% of the media. The formation, integrity, diameter, and volume of the MCTS were monitored by a DMi1 inverted phase contrast microscope (Leica Microsystems). The volumes were calculated using the equation $V = 4/3\pi r^3$.

2.3.5. Cell death induction assays

Cell death induction of the nanocapsules on HeLa cells was determined by dual FITC-Annexin V/Propidium Iodide (PI) labelling method *via* flow cytometry. Briefly, HeLa cells were seeded in 12-well plates at a density of $1.5\cdot10^5$ cells/well and incubated overnight. Testing treatments were added at indicated concentrations for 24 h and cisplatin was used as a

positive control for apoptosis induction. After treatment, cells were harvested by trypsinization, washed with binding buffer, centrifuged and the pellets were resuspended in 185 μL binding buffer (Roche). Then, 5 μL Annexin-V-FLUOS and 10 μL PI were added and the resuspended cell solution was left at room temperature in the dark for 15 min. Cells were analyzed by flow cytometry (Beckton Dickinson FACSCalibur), 10^4 events acquired in each sample by registering at 620 and 525 nm for PI and Annexin V, respectively, $\lambda_{exc}= 488$ nm. Data were analyzed using FlowingSoftware version 2.5.1. The assay was performed in three independent experiences (n= 2 per replicate) yielding similar results.

2.3.6. Morphological analysis of cells

Cell morphology of HeLa cells upon treatment was determined by flow cytometry. Briefly, HeLa cells were seeded in 12-well plates at a density of $1.5 \cdot 10^5$ cells/well and incubated overnight. Testing treatments were added at indicated concentrations for 24 h and cisplatin was used as a positive control for apoptotic changes induction. After treatment, cells were harvested by trypsinization, washed with binding buffer, centrifuged and the pellets were resuspended in PBS. Samples where then subjected to flow cytometry (Beckton Dickinson FACSCalibur), where 10^4 events were acquired per sample by plotting FSC-H (cell size) vs. SSC-H (cell complexity). Data were analyzed using FlowingSoftware version 2.5.1. The assay was performed in two independent experiences (n= 2 per replicate) yielding similar results.

2.3.7. Cell membrane integrity test

HeLa cells were seeded in 12-well plates at a density of $1.5 \cdot 10^5$ cells/well. After overnight incubation, treatments were added at indicated concentrations for 24 h. Then, cells were harvested by trypsinization and the pellets were resuspended in propidium iodide solution (20 μg/mL) for 15 min. Samples where then subjected to flow cytometry (Beckton Dickinson FACSCalibur). 10^4 events were acquired per sample in FL2-H channel. Data were analyzed using FlowingSoftware version 2.5.1. The assay was performed in three independent experiences (n= 2 replicates).

2.3.8. Mitochondrial potential assessment

Mitochondrial membrane potential was evaluated with the fluorescent probe JC-1 chloride (Promocell). HeLa cells in the density of $1.5 \cdot 10^5$ were seeded for 24 h in complete medium on 12-well plates, and then treated with indicated concentrations of tested compounds for 24 h. Untreated cells contained maximal concentration of DMSO used in the treatment (0.4%) and were used as a negative control, whereas Antimycin A (50 μM) was used as a positive control

for mitochondrial dysfunction. After drug exposure, the cells were incubated with JC-1 dye (1 µM) for 20 min and subjected to flow cytometry (FACSCAlibur BecktonDickinson; 10^4 events acquired per sample), using λ_{exc}= 488 nm and registering emission in the range 430-600 nm to discriminate green JC1 monomers (FL1-H channel) and red JC1 aggregates (FL2-H channel). Three independent experiments were performed (n=2 replicates).

2.3.9. Aerobic respiration and glycolytic rate evaluation

The mitochondrial OXPHOS and glycolysis function of HeLA cells was measured by determining the oxygen consumption rate (OCR) and extracellular acidification rate (ECAR) in real-time with Seahorse XFe96 extracellular flux analyzer. HeLA cells were seeded at a density of $3 \cdot 10^4$ cells/well to the XFe96-well culture microplates (Seahorse Agilent) the day before. The sensor cartridge was hydrated through immersion on calibration buffer at 310 K in a non-CO_2 incubator overnight. Buffered DMEM (Seahorse Bioscience) was used for glycolysis test prior to the assay. Cells were treated for 24 h at indicated concentrations with testing compounds. Then cell metabolism was assessed using XF Glycolytic Rate Test Kit. Different parameters were calculated by subtracting average respiration rates before and after the injection of a mixture of complex III electron transport chain inhibitors (Rotenone/Antimycin A, 1 µM) and glycolysis inhibitor (2-deoxyglucose, 50 mM). Each test had four replicates.

2.3.10. Oxidative stress induction

Briefly, HeLa cells were seeded in 12-well plates at $1.5 \cdot 10^5$ cells/well and treated for 24 h with nanoparticles at indicated concentrations; cisplatin (20 µM) was used as positive control for DNA damage induction. Cells were then collected by trypsinization, fixed in 400 µL 0.2 % paraformaldehyde for 5 min and permeabilized with Triton X 0.5 %. After fixation and permeabilization, a 3 % FBS solution containing 0.6 µg/mL anti-pH2AX (ser139) FITC-conjugated monoclonal antibody (CR55T33, eBioscience™) was added and incubated for 1 h at room temperature avoiding direct light. Cells were then analyzed using Beckton Dickinson FACSCalibur flow cytometer with 10^4 acquisitions per sample and registering FL1-H channel, λexc = 488 nm. Three independent experiments with n=3 were performed.

3. RESULTS AND DISCUSSION

3.1. Synthesis of Ir(III) complexes.

Ir(III) complexes **Ir1** and **Ir2** were synthesized in the thermodynamically favored *fac*-configuration. The first step consisted of the synthesis of the dimer, $[Ir(C^\wedge N)_2(\mu-Cl)_2]$, by reaction of $IrCl_3 \cdot H_2O$ with 2-phenyl-1-[4-(trifluoromethyl)benzyl]-1H-benzo[d]imidazole (Scheme S1), which was previously synthesized.[28] Homoleptic complex **Ir1** was synthesized in a good yield (65%) by reaction of $[Ir(C^\wedge N)_2(\mu-Cl)_2]$ with an excess of the ligand, using a high boiling point solvent (2-ethoxyethanol) and silver triflate to extract the chlorides (Scheme S2).[29] On the other hand, heteroleptic complex **Ir2** was synthesized by reaction of the dimer with commercially available 2-phenyl-1H-benzo[d]imidazole in reflux of 2-ethoxyethanol for 3 hours using sodium carbonate (Scheme S3).[30] The product of this reaction was a mixture of the three possible neutral compounds: the previously synthesized $[Ir(C^\wedge N)_3]$ **Ir1**, $[Ir(C^\wedge N)_2(C'^\wedge N')]$ **Ir2** and $[Ir(C^\wedge N)(C'^\wedge N')_2]$ (Scheme S4), being **Ir2** the main component of the mixture. Similar behaviour was previously described.[33] Pure heteroleptic complex **Ir2** was isolated by silica column chromatography as the retention factor (Rf) depends on the number of NH groups of the complexes. **Ir2** was eluted in second place (31%), preceded by the complex **Ir1** (9%) and finally, the most retained product $[Ir(C^\wedge N)(C'^\wedge N')_2]$ (13%) (Scheme S4).

All investigated complexes were fully characterized by ^1H and ^{13}C NMR spectroscopy (Figures S1 and S3), positive-ion ESI-HRMS (Figure S2 and S4) and elemental analysis. The *fac-mer* configuration of the complexes was assigned using ^1H-NMR. In *fac*-tris-cyclometalated homoleptic **Ir1**, the three $C^\wedge N$ ligands surrounding the central atom are magnetically equivalent due to C3 symmetry of the compounds. This makes the total number of resonances equal to the number of resonances of a single $C^\wedge N$ ligand.[34] The signals in the ^1H-NMR spectrum of **Ir1** (Figure S1) correspond to 14 protons of three equivalent benzimidazole-based ligands. Recently, *fac* isomerism has been assigned to Ir(III) heteroleptic complexes with phenylpyridine ligands based on the synthesis temperature (~ 135 °C) and the simplicity of their ^1H-NMR spectra.[35] In our case, given the impossibility of obtaining valid monocrystals of **Ir2** for X-ray diffraction, the *fac* configuration was assigned for these complexes based on the ^1H-NMR spectrum (Figure S3) and the temperature of the synthesis. In both cases, the positive-ion ESI mass spectra exhibited the expected molecular ion (Figure S2 and S4).

3.2. Synthesis and characterization of Ir(III)-loaded nanocapsules.

The synthesis of Ir(III) complex-loaded nanocapsules involved two main processes, as shown in Scheme 1: the preparation of an amphiphilic polyurethane-polyurea amino terminal-reactive prepolymer (steps 1-3) and the metallodrug nanoencapsulation (steps 4-7). First, polymerization between the diol and the diisocyanate monomers afforded a reactive NCO-terminated pre-polymer (step 1). When the theoretical % of isocyanate groups was reached, the polymer was dissolved in THF and added dropwise over a slightly excess of an hydrophobic diamine solution (step 2) to end-cap it with primary amines (step 3), which allows the storage of this intermediate avoiding moisture-promoted degradation due to NCO water sensitivity. This reaction was monitored by FT-IR until the complete disappearance of the NCO stretching band around 2250 cm^{-1} (Figure S5). For the nanoencapsulation process, the NH$_2$-terminal polymer was reactivated with an excess of a diisocyanate derivative in THF and the Ir(III) complexes (**Ir1** or **Ir2**) were added to this organic solution (step 4). Once confirmed the presence of isocyanate groups by FT-IR (Figure S6), a basic solution of L-lysine was added dropwise under mechanical stirring, forming a water-in-oil nanoemulsion (step 5). Then, the phase inversion was triggered by addition of a fixed amount of water (step 6) followed by the addition of diethylenetriamine, which rapidly resulted on crosslinked cyclometalated Ir(III) complex-loaded polyurethane-polyurea hybrid nanocapsules (**NC-Ir1** and **NC-Ir2**) (step 7). Both Ir(III)-containing nanocapsules as well as control nanocapsules lacking the metallodrug cargo (**NC-GTCC**) were purified by dialysis using a molecular porous membrane tubing with a 12–14 kDa MWCO. As shown in Figure 2, the introduction of both PEGylated and ionomeric groups, together with core-oriented lipophilic tails for solubilizing and stabilizing the metallodrug through hydrophobic interactions, defines the stratification of the shell. This structure provides a stable aqueous suspension of the nanocapsules exhibiting distinctive biological performance, such as long-circulation in blood stream and specific accumulation in acidic TME.[17,36] In addition, the incorporation of disulphide bonds in the polymer backbone allows the specific biodegradation of the system under reductive conditions, which would facilitate the release of the Ir(III) metallodrugs.[17]
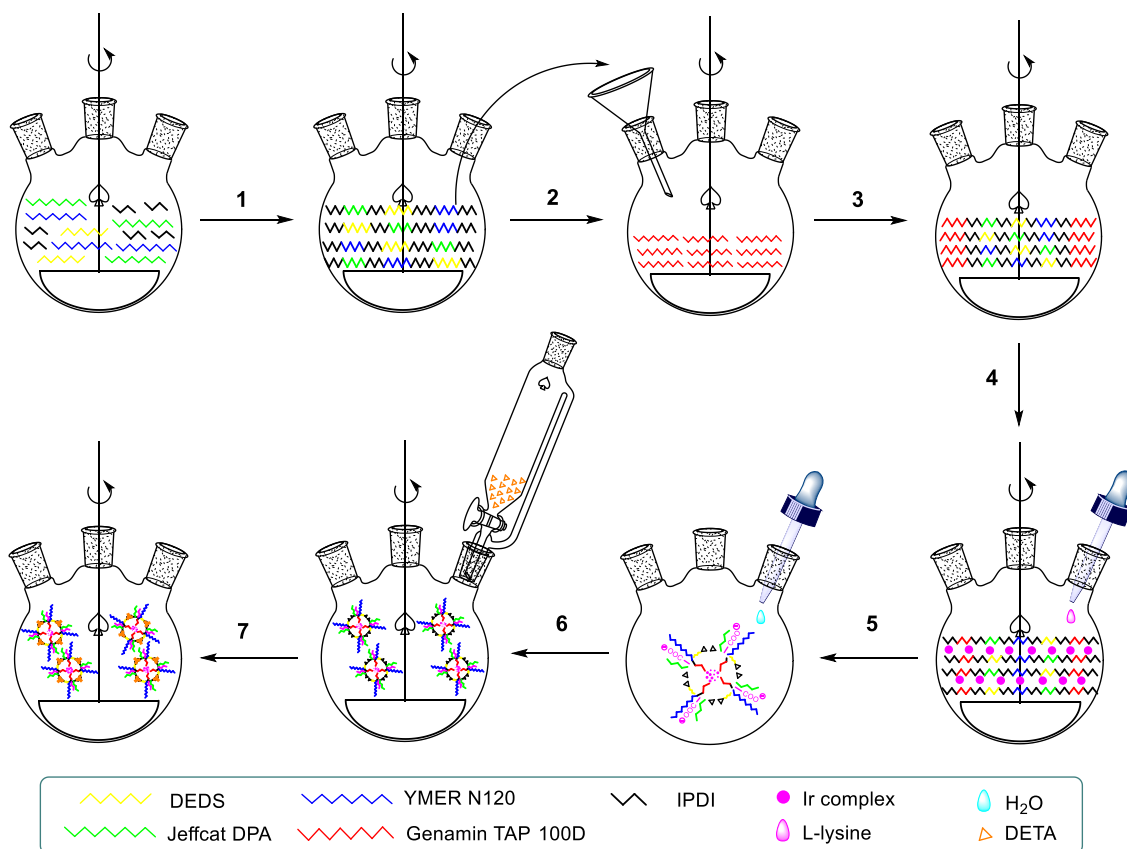
Scheme 1. Schematic representation of the preparation of the amphiphilic prepolymer (steps 1-3) and of the nanoencapsulation process (steps 4-7). Abbreviations: 2,2´-dihydroxyethyl disulfide (DEDS), N-(3-dimethylaminopropyl)-N,N´-diisopropanolamine (DPA), isophorone diisocyanate (IPDI), 1,3-diamino-N-octadecylpropane (Genamin TAP 100D), diethylenetriamine (DETA).

The size of the Ir(III) complex-loaded nanocapsules (**NC-Ir1** and **NC-Ir2**) was studied by dynamic light scattering (DLS) and compared with that of the non-loaded NCs (**NC-GTCC**). As shown in Figures 2 and S7-S9, the average particle size distribution was centered approximately at 18 nm for **NC-Ir1/Ir2**, which was of the same order than that of non-loaded NCs (22 nm). In all cases, the standard deviation (SD) was very low (Table S3). The morphology of **NC-Ir1** and **NC-Ir2** was also studied by Transmission Electron Microscopy (TEM), and a roughly round shape and homogeneous particle size was revealed by TEM micrographs (Figures 2 and S10-S11). Although nanocarriers with size around 100 nm are usually designed to facilitate accumulation at the tumor site by the enhanced and permeability and retention effect (EPR),[37] smaller nanomedicines (e.g. 15-20 nm) such as the Ir(III)-loaded NCs might be preferred for cancer therapy due to their higher tumor penetration.[38]

The Z-potential of the nanocapsules at different pH values (6.5, 7.0 and 7.5) was also measured to evaluate the pH-dependent amphoteric properties of the polymeric shell. As shown in Table S4 and Figure S12, the nanocapsules are slightly anionic under physiological conditions (pH = 7.4), particularly those containing the heteroleptic complex **Ir2**, but become cationic at low pH values. This is an important property since ensures long circulation half-life in the blood stream, thereby allowing slow accumulation into abnormally vascularized tumor tissues where the relatively acidic environment (pH = 5.8-6.9) triggers NCs to become cationic entities and, consequently, with high internalization ability via association with negatively charged cell receptors.[39]

The amount of Ir complexes (**Ir1** and **Ir2**) inside the NCs was determined by ICP-MS analysis. As shown in Table S5, the encapsulation efficiency was relatively high in both cases (*ca* 40 %) considering that no external surfactants were used, and high loading of both hydrophobic Ir(III) complexes was obtained (e.g., 130 ± 16 μM in **NC-Ir1** and 206 ± 17 μM in **NC-Ir2**).
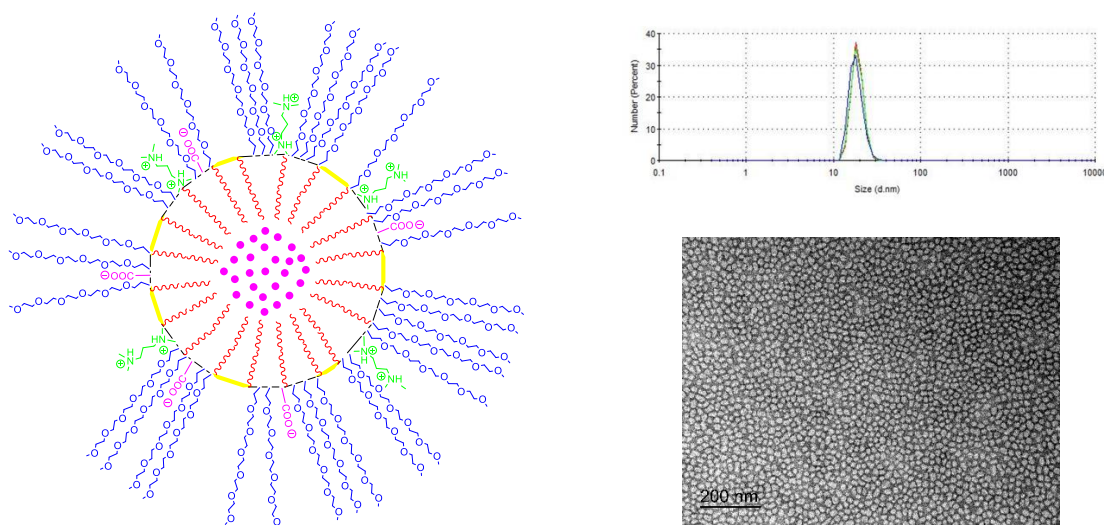

Figure 2. Left: schematic representation of the structure of a metallodrug-loaded nanocapsule, showing the orientation of the hydrophilic and hydrophobic tails of the prepolymer in a simplified way. It is expected to have multilayers self-stratified at the interface metallodrug/water in a gradient from inside to outside the nanocapsule wall driven mainly by hydrophobic interactions. Right: particle size distribution measured by DLS (top) and TEM micrograph (bottom; scale bar: 200 nm) of **NC-Ir1**.

Once confirmed that the Ir(III)-loaded NCs exhibited an adequate size and a relatively high Ir(III) complex loading, we focused on investigating their ability to specifically release the metallodrug cargo into cancer cells under reductive conditions as well as their stability. The latter is particularly important to avoid premature degradation and unspecific leakage of the metallodrug in the blood stream. It is well-known that the ratio of the reduced form of glutathione (GSH) *versus* the oxidized form (GSSG) is considerably higher in solid tumors cells than in healthy ones, being the intracellular concentration of GSH in the cytosol (2–10 mM) much higher than in the blood or in the extracellular matrix (2–20 μM).[40] This upregulation in cancer cells derives from the overproduction of this antioxidant tripeptide, on account of different biological mechanisms,[41] to mitigate the oxidative stress which they are exposed to, allowing proliferation and, in most cases, enabling multidrug resistance (MDR).[42] The enhanced level of reduced glutathione is not exclusively, but thoroughly observed in solid tumor cells. For this reason, many nanomedical devices have taken advantage of this fact to selectively release anticancer drugs in the tumor microenvironment.[43] In our case, disulfide bonds were incorporated in the polymeric wall to trigger degradation of the NCs by reductive enzymes and peptides overexpressed in the cytosolic environment of tumor cells and, consequently, the release of the metallodrug cargo.

The disruption of the polymeric wall via GSH-mediated disulfide bond reduction was investigated by TEM analysis after incubation of **NC-Ir2** for 2, 24 and 48 h at 37ºC in GSH-supplemented PBS (10 mM).[44] As shown in Figure S13, Ir(III)-loaded NCs maintained their morphology when they were incubated in PBS and the analyzed fields remained homogeneous, with no variations in terms of morphology or distribution along the screening. However, the amount of NCs clearly diminished over time, at the same magnification analysis, when incubation was carried out in GSH-containing buffer, which suggests that **NC-Ir2** suffer degradation through reduction of disulfide bonds incorporated along the polyurethane backbone of the NCs wall. It is also worth noting that **NC-Ir2** modified their morphology after incubation for 48 h in GSH-supplemented PBS, mostly disappearing the 20-25 nm spherical structures and forming non-defined aggregations (Figure S14), which can be associated with clusters of polymer and precipitation of the free **Ir2** complex after being released.

Additionally, the stability of the NCs was also evaluated in PBS containing BSA, which is one of the most abundant proteins in plasma, as well as in complete Human AB Serum. As shown in Figure S15, **NC-Ir2** showed a clear spherical morphology and proper distribution

after incubation for 48 h both in BSA-containing PBS and in Human AB Serum, confirming the high stability of polyurethane, polyurea and disulfide bonds under common medical vehicles and human bloodstream medium, making them a suitable tool for intravenous administration.

3.3. Photophysical properties

The UV/Vis absorption and emission spectra were recorded in CH_2Cl_2 and DMSO for Ir(III) complexes (Figure S16) whereas water solutions were used for the nanocapsules (Figure 3). **Ir1** and **Ir2** exhibit characteristic absorptions of tris-cyclometalated iridium complexes.[45] The luminescence lifetimes and emission quantum yields are summarized in Table S6. The luminescence lifetimes of **Ir1** and **Ir2** go from being nanoseconds in aerated solution to microseconds in degassed solution (Table S6 and Figure S17). These long-lived excited states compare well with the respective values for other phosphorescent Ir(III) compounds, which supports the triplet nature of the emission state.[45ab] Likewise, the luminescence lifetimes of **NC-Ir1** and **NC-Ir2** increased from ~70-90 ns in air equilibrated solutions to ~1.5 µs, in degassed solutions (Table S6 and Figure S18), as it happened with the free complexes in CH_2Cl_2.
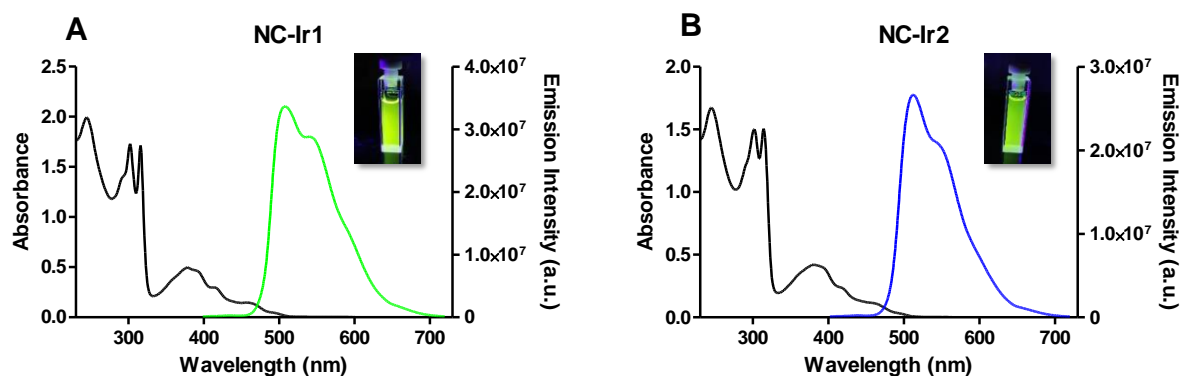

Figure 3. UV/Vis and emission spectra in aerated water solutions of A) **NC-Ir1** (λ_{exc}= 378 nm) and B) **NC-Ir2** (λ_{exc}= 382 nm).

This fact together with their similar spectra to that registered for **Ir1** and **Ir2** in CH_2Cl_2, is a good indicative of the hydrophobic environment generated by the nanocapsules. On the other hand, both complexes and nanocapsules exhibited high emission quantum yields in solution. Unlike free complexes, which were easily quenched by oxygen, the oxygen quenching of the

emission was less efficient when the complexes were encapsulated within the nanoparticles. While the emission quantum yields of **Ir1** and **Ir2** in an air-equilibrated solvent ($\Phi_{air} \approx 3\%$) have a 30-fold reduction in luminescence features with respect to degassed solutions ($\Phi \approx 78\%$), **NC-Ir1** and **NC-Ir2** showed a smaller difference between aerated ($\Phi_{air} \approx 20\%$) and degassed ($\Phi \approx 40\%$) solutions. Interestingly, the nanocapsules displayed quantum yields of 12-20% in aerated aqueous solution, which indicated that these nanostructures can be used in the presence of dissolved oxygen and still exhibit a high quantum yield.

3.4. Biological activity of NC-Ir1 and NC-Ir2.

3.4.1 Cellular uptake in cancer cells.

The cellular uptake of Ir(III) complexes either alone or loaded into NCs was investigated in cervical cancer cells (HeLa) using inductively coupled plasma mass spectrometry (ICP-MS). As shown in Figure 4, after 2 h incubation the iridium content inside cancer cells treated with **Ir1** and **Ir2** at 6 µM was much lower than that found with Ir(III) complex-loaded nanocapsules at the same concentration, especially in the case of the homoleptic complex. Indeed, Ir accumulation from **NC-Ir1** and **NC-Ir2** was 6- to 14-fold higher than those found in HeLa cells treated with the free complexes **Ir1** and **Ir2**, respectively, thus indicating that encapsulation in polyurethane-polyurea hybrid NCs allowed neutral Ir compounds to be rapidly internalized in the cells. Once attached to cell surface, these nanoparticles might passively diffuse to cells through the lipid membrane or translocate via endocytosis-mediated transport. Whereas at 37 ℃ both passive and active transport across the membrane would be operative, at 4 ℃ energy-dependent transport processes are generally unable to function, and only passive diffusion or cell membrane adhesion will be operational. Since decreasing temperature from 37 ℃ to 4 ℃ significantly reduced cellular uptake of Ir(III)-loaded NCs after 2 h (Figure 4), energy-dependent transport could be partially responsible for the increased accumulation at physiological temperature of **NC-Ir1** and **NC-Ir2**.
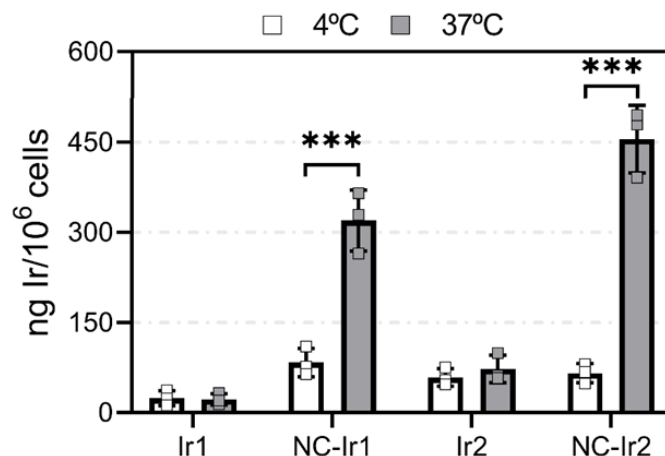
Figure 4. Intracellular accumulation of Ir after 2 h with free or encapsulated compounds (6 µM) determined by ICP-MS in HeLa cells. Data expressed as mean ± SD of three independent measurements (***p<0.001; unpaired *t*-test).

Confocal microscopy in living HeLa cells was also used to investigate the cellular uptake of the compounds. As shown in Figure S19, luminescent aggregates of **Ir1** and **Ir2** were observed outside the cells due to the low solubility in water of the compounds. This fact is in good agreement with the ICP-MS results and confirms the poor cellular uptake of the free iridium complexes. By contrast, intracellular staining was observed after incubation with **NC-Ir1** and **NC-Ir2** (Figure S20), thereby confirming an excellent cellular uptake of the Ir(III)-loaded NCs.

3.4.2. Antiproliferative activity in 2D and 3D cell culture models.

The cytotoxic activities of Ir(III) complexes alone or encapsulated into polyurethane-polyurea hybrid NCs were tested against three 2D monolayer cancer cells by means of MTT-based assays (cervical cancer cells (HeLa), ovarian cancer sensitive (A2780) and resistant to the clinical drug cisplatin (A2780cis), as well as in non-tumorigenic normal renal cells (BGM). **Ir1** and **Ir2** compounds were found to be inactive against cells up to 100 µM (data not shown), which is in good agreement with ICP-MS studies that showed very low intracellular uptake of these compounds. In contrast, treatment with **NC-Ir1** and **NC-Ir2** resulted in high antiproliferative activity against cancer cells while cells treated with non-loaded NCs did not (Tables 1 and S7). This indicated that the cytotoxic action of the iridium(III) compounds greatly improved upon encapsulation. Overall, viability of HeLa cells was affected by **NC-Ir1** and **NC-Ir2** treatment after 2 h and was further decreased after 24 h and 48 h, which could be

attributed to a higher release of the Ir(III) complex cargo over time, as suggested by TEM analysis (Figures S13-S14). The NCs were also active against ovarian cancer cells, showing remarkable antiproliferative activities in both cisplatin sensitive and resistant cell lines after 24 h, whereas an absence of cytotoxicity was observed in BGM, thus indicating the ability of NC-loaded agents to preferentially eliminate cancer cells over normal dividing cells.

Table 1. Cytotoxicity [IC_{50} mean values (µM)][a] obtained for nanoparticles in cancer and normal cells based on the loaded metal concentration (Ir for **NC-Ir1** and **NC-Ir2**; Pt for cisplatin).

	HeLa			A2780	A2780cis	BGM
	2 h	24 h	48 h		24 h	
NC-Ir1	23 ± 1	2.9 ± 0.2	1.77 ± 0.06	3.7 ± 0.9	10 ± 1	>85
NC-Ir2	47 ± 6	3.6 ± 0.2	2.9 ± 0.1	2.5 ± 0.6	9.8± 0.9	>85
Cisplatin	-	-	33 ± 6	1.4 ± 0.2	16 ± 1	16.6 ± 0.2

[a] The results are expressed as mean values ± SD from at least two independent experiments (n=4). The terms >85 indicate that no IC_{50} was reached up to that concentration.

The tumor growth inhibition effects of the complexes were also tested in multicellular HeLa tumor spheroids (MCTS). Three-dimensional MCTS models provide an *in vitro* cell culture system which mimics the *in vivo* features of solid tumors and represent a simplified approximation of the tumor microenvironment,[46] thereby allowing a more realistic evaluation of the antitumor activities of the nanoparticles. **NC-Ir1** and **NC-Ir2** were incubated with MCTS after their formation and either fresh media or treatment-containing media were replaced every 3 days. Over a span of 15 days, period, shape, diameter and volume of the MCTS were monitored. In contrast to the control, the size of the spheroids did not increase in treated groups, indicating the ability to impair tumor growth in these 3D models (Figure 5 and Figure S21). This effect was maintained after 15 days of treatment, with shrank and disaggregated MCTS, demonstrating a strong tumor growth inhibition effect.
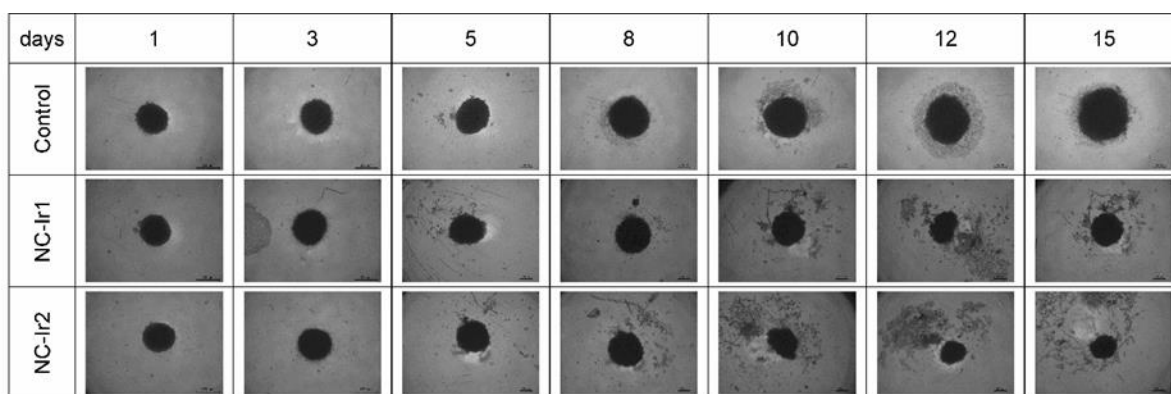
Figure 5. Changes in relative volume in MCTS over a span of 15 days. MCTS were treated with **NC-Ir1** and **NC-Ir2** at 6 μM. Scale bar: 200 μm.

3.4.3. Morphological alterations of the cells.

In order to determine the mechanisms responsible for the cytotoxic effects of the Ir(III)-loaded nanoparticles, confocal microscopy and flow cytometry techniques were first applied to observe the morphological alterations in HeLa cells. HeLa cells in culture appear as flattened epithelioid cells well-adhered to the surface. However, examination of these cancer cells after incubation with **NC-Ir1** and **NC-Ir2** revealed swollen cells that became rounded in shape and detached from substrate shortly after treatment, *i.e.* ~12 h (Figure 6). This effect, which might indicate cell death being induced, was prolonged after 24 h (Figure S22). Some of the cells also started to produce blebs in their cell membrane (Figure S23), which allowed us to rule out paraptosis as the main cell death mode since neither swelling nor blebbing are associated to paraptosis.[47] Flow cytometry experiments using forward and side scatter plots (FSC and SSC) to discriminate cell size and cell complexity respectively were performed (Figure S24). In contrast to cisplatin-treated cells, which showed a decrease in FSC and a concomitant increase in SSC parameters corresponding apoptotic populations, cells treated with **NC-Ir1** and **NC-Ir2** revealed a main population of cells with increased size, which would confirm the cell swelling, and a second population of small cell particles defined by low FSC/SSC ratios corresponding to dead cells.
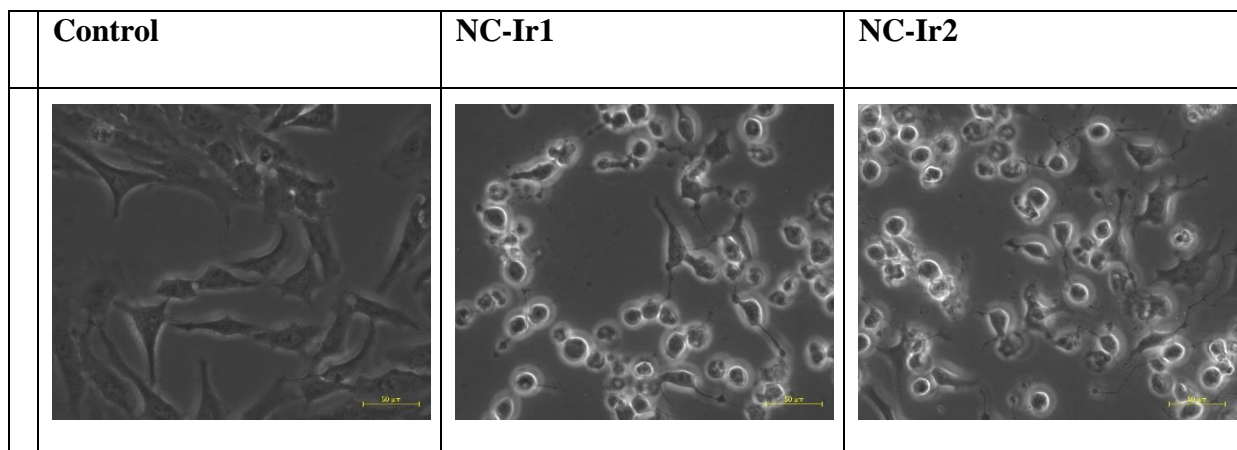
Control	NC-Ir1	NC-Ir2

Figure 6. Detection of cell swelling in HeLa cells after 12 h treatment with nanoparticles at equitoxic concentrations ($2 \times IC_{50}$; *i.e.* 6 μM). Scale bar: 50 μm.

3.4.4. Cell death induction by NC-Ir1 and NC-Ir2.

To elucidate the mode of cell death induced by NCs loaded with Ir(III) compounds, flow cytometry experiments using a Annexin V/Propidium Iodide (PI) labelling method were performed. This dual-staining allowed the detection of four different populations: live cells, necrotic cells and early- and late-stage apoptosis. Although apoptosis is characterized by changes in phospholipid membrane symmetry, the disruption of the cell membrane integrity allows the detection of necrotic cells as they become permeable to PI. In the case of HeLa cells exposed to 20 μM of cisplatin, which served as a positive control, PI^+ and double Annexin V^+/PI^+ populations were induced, revealing apoptosis and necrosis induction after 24 h (Figure 7). Treatment with **NC-Ir1** and **NC-Ir2** also increased both Annexin V^+ and PI^+ populations; the latter being significantly produced. Overall, these results suggested that necrotic events in HeLa cells may be induced upon treatment.
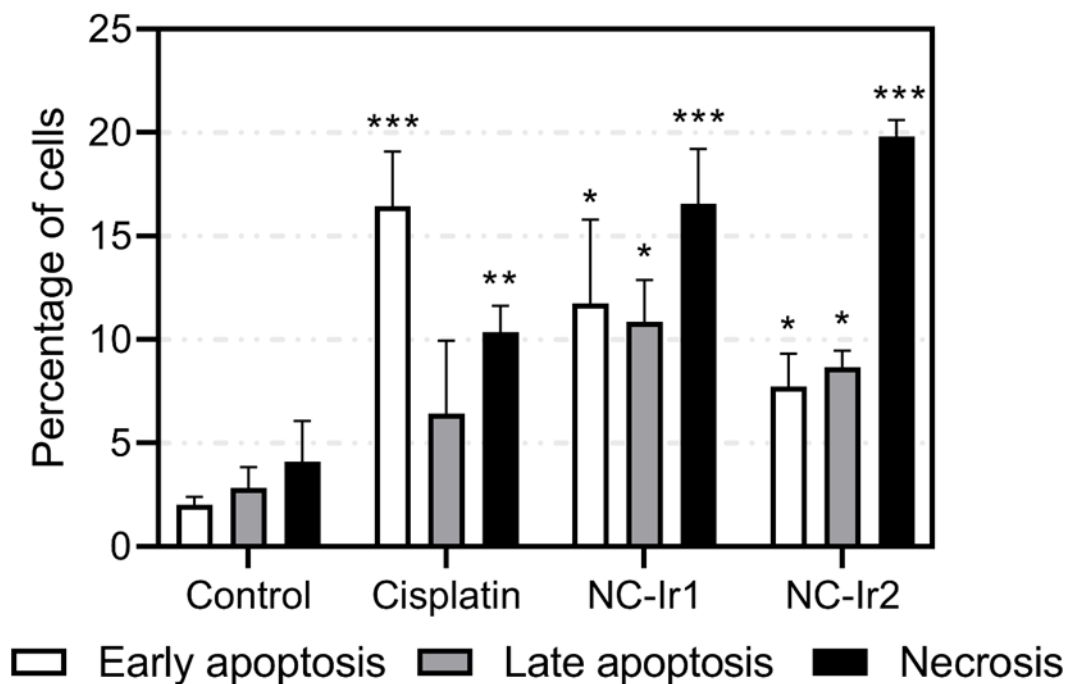
Figure 7. Cell death induction in HeLa cells after 24 h treatment with **NC-Ir1** and **NC-Ir2** (6 μM) or cisplatin (20 μM). Data expressed as mean ± SD from three independent experiments (*$p<0.05$, **$p<0.01$, ***$p<0.001$; unpaired t-test).

Cells with compromised plasma membrane would allow PI to permeate into cytoplasm and intercalate to DNA. Therefore, detection of PI fluorescence by flow cytometry would allow the evaluation of cancer cell membrane integrity upon low-dose treatments with the nanoparticles (Figures S25 and 26). **NC-Ir1** and **NC-Ir2** for 12 h was sufficiently enough to affect membrane permeability and thereby induce loss of plasma membrane integrity. This was confirmed by confocal microscopy after staining with PI (Figure 8). The observed changes in cell morphology (cell swelling, blebbing and disruption of membrane integrity) were coherent with those found on FSC-SSC analysis, characterized by a reduction of cell size and complexity (Figure S22). Altogether, the onset of morphological events appeared to be consistent with oncosis or oncotic necrosis.[48]
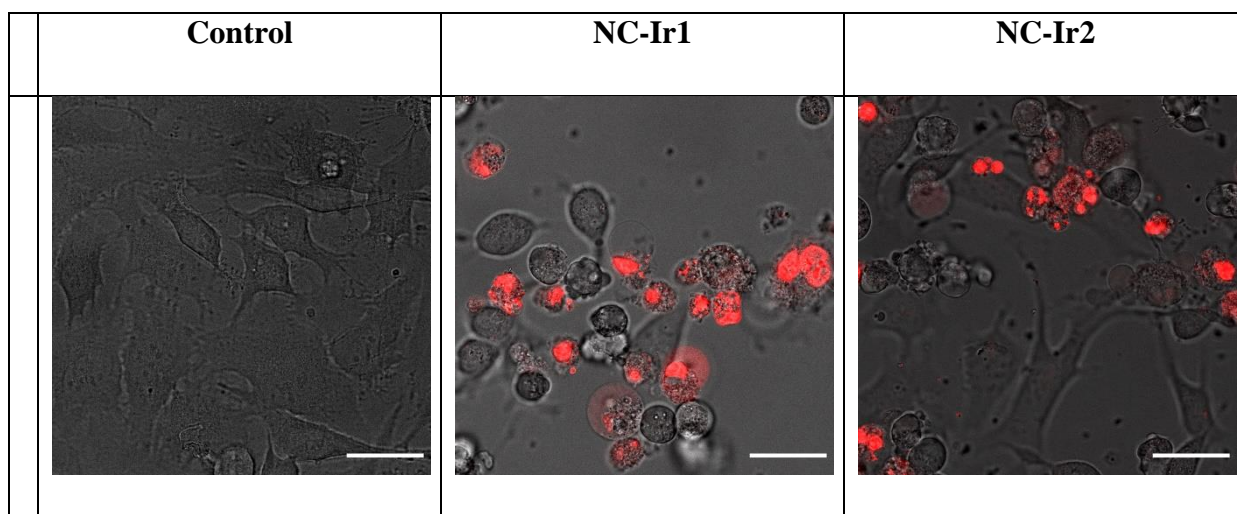
| Control | NC-Ir1 | NC-Ir2 |

Figure 8. Microscopy images of HeLa cells with membrane rupture stained with propidium iodide (red) after treatment with **NC-Ir1** and **NC-Ir2** at equitoxic concentrations ($2\times IC_{50}$; *i.e.* 6 μM) for 12 h. Scale bar = 15 µm.

3.4.5. Mitochondrial dysfunction.

Since mitochondria play an important role in biological processes of cancer cells, including redox homeostasis and ATP production,[49] a series of experiments were performed to investigate the impact of the present encapsulated agents on mitochondrial dysfunction. First, the effects on mitochondrial membrane potential (MMP) were evaluated after 24 h treatment with Ir(III)-loaded NCs using JC-1 staining. JC-1 dye exhibits bright red fluorescence signal upon potential-dependent accumulation in healthy mitochondria, whereas a shift to green fluorescence is observed if dissipation of MMP occurs. Similar to the electron transport chain inhibitor antimycin A, treatment with **NC-Ir1** and **NC-Ir2** completely depleted the MMP of HeLa cells after 24 h (Figures 9 and S27).
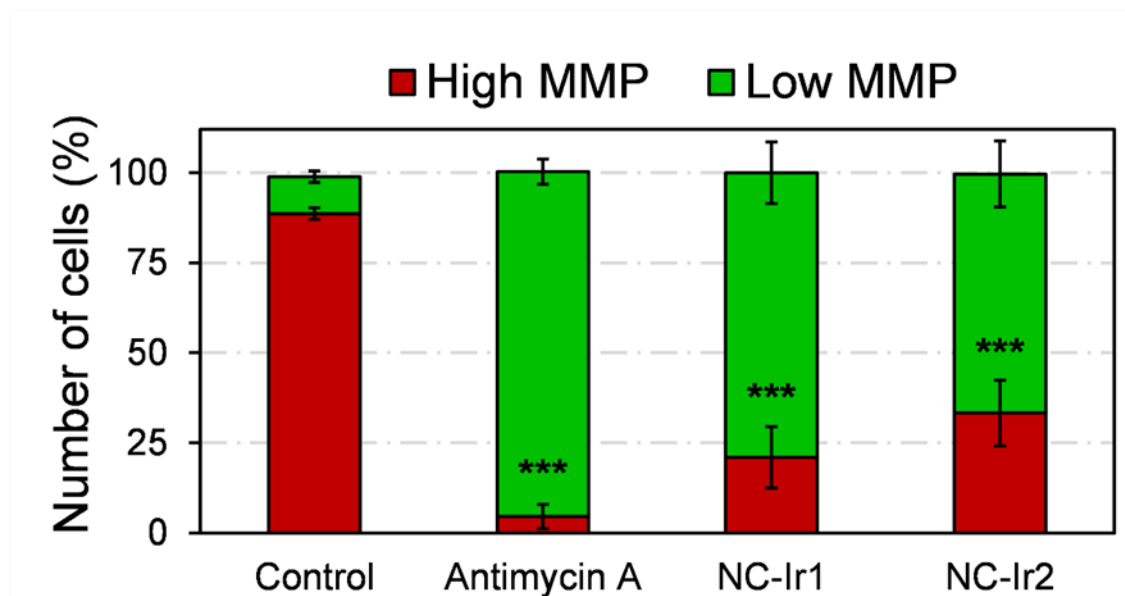
Figure 9. Mitochondrial membrane potential (MMP) of HeLa cells after treatment with antimycin A (50 µM) **NC-Ir1** and **NC-Ir2** (6 µM) for 24 h. (*p<0.05, **p<0.01, ***p<0.001; unpaired t-test).

To further understand how mitochondrial bioenergetics were affected, extracellular acidification (ECAR) and oxygen consumption rates (OCR) were measured in real-time using a Seahorse XF-96 flux analyzer. As depicted in Figures S28, the administration of **NC-Ir1** and **NC-Ir2** (6 µM) resulted in evident suppression of the glycolytic rate and mitochondrial respiration. On the one hand, HeLa cells incubated with Ir(III)-loaded NCs led to a suppression on OCR compared to **Ir1** and **Ir2**-treatments, which increased mitochondrial oxidative phosphorylation, thus showing the ability of the encapsulated agents to impair mitochondrial function (Figure S28a). On the other hand, it is generally accepted that cancer cell metabolism is commonly shifted from mitochondrial respiration to aerobic glycolysis in what is known as Warburg effect.[50] Ir(III)-loaded NCs abolished the glycolytic rate of HeLa cells, both basal glycolysis and compensatory glycolysis, as evidenced by reduced ECAR under basal conditions and after injection of mitochondrial respiratory chain inhibitors Rotenone/Antimycin A (Figure S28b-d). Different from them, no influences on acidification rates were found when treated with **Ir1**, **Ir2** or cisplatin under the same conditions. Overall, these results suggest that treatments with **NC-Ir1** and **NC-Ir2** altered cancer cell metabolism by suppressing glycolysis and decreasing mitochondrial oxidative phosphorylation activity. Taking into account that iridium barely entered into cancer cells when administered as free compounds compared to encapsulated administration (see Figures 4 and S19-S20), such

differences in the biological effects could be attributed to the lower internalization of the free Ir(III) complexes rather than different intracellular distribution.

3.4.6. Oxidative stress.

Mitochondria are the major cellular source of reactive oxygen species (ROS) within cells. Since mitochondrial dysfunction can result in an elevation of ROS levels,[51] we decided to assay the effect of canonical ROS on DNA damage as a marker of oxidative stress in cancer cells. Extensive ROS production can generate double-strand breaks in DNA that can be detected by using fluorescently labeled anti-γH2AX antibody specifically targeted to phosphorylated Ser139 of the variant of histone H2A. Our results showed that DNA damage was slightly induced by low-dose treatment ($0.5 \times IC_{50}$; *i.e.* 1.5 μM) with **NC-Ir1** and **NC-Ir2**, and more broadly at $2 \times IC_{50}$ concentrations after 24 h (Figure 10 and Figure S29). Strikingly, treatment with these concentrations significantly raised γH2AX populations as it did the well-known damaging agent cisplatin. This led us to think that oxidative stress might be contributing to the mechanism of action of the present Ir(III)-loaded nanoparticles, probably as a result of mitochondrial dysfunction.

To further confirm that ROS generation was a main contributor of the nanoformulation cytotoxicity, the influence of an exogenously-added antioxidant was studied. As presented in Figure S30, pretreatment of HeLa cells for 1 h with the cell permeable superoxide dismutase mimetic, MnTBAP, attenuated the nanoparticle-induced cytotoxicity at $2 \times IC_{50}$ concentrations for 24 h. The compensatory effects on cell viability exerted by this antioxidant supports the idea of extensive ROS generation being produced by these Ir-loaded nanocapsules.
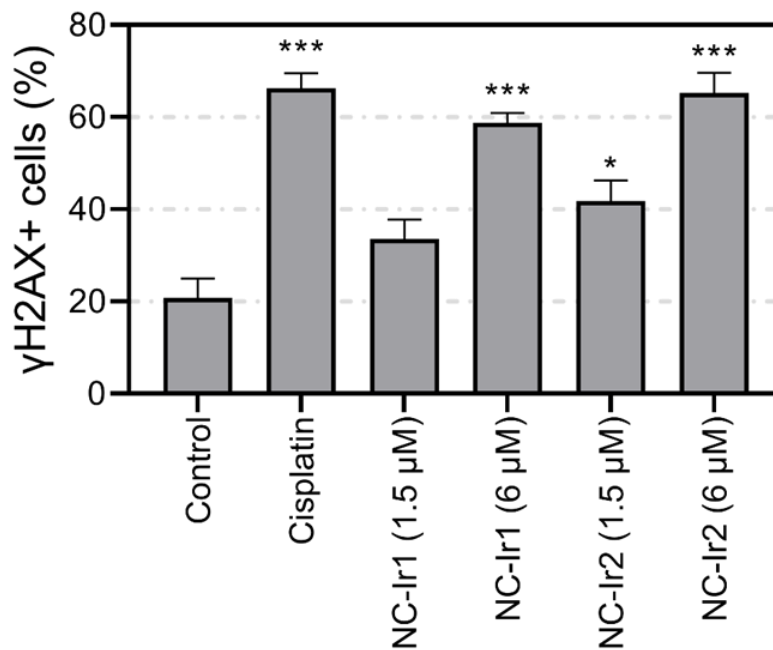
Figure 10. Effect of **NC-Ir1** and **NC-Ir2** (1mg/ml) on oxidative stress of HeLa cells as measured by DNA damage detected as changes in γH2AX phosphorylation in the FL1-H channel after 24 h treatment. Cisplatin (20 µM) was used as a positive control for DNA damage induction. Data from three independent experiments (n=3 replicates).

4. CONCLUSIONS

In summary, we have demonstrated for the first time that polyurethane-polyurea hybrid nanocapsules can be used to efficiently encapsulate hydrophobic metallodrugs under aqueous conditions, which opens the way to the development of novel metal-based anticancer nanomedicines. As a proof of concept, we have encapsulated two neutral phosphorescent tris-cyclometalated Ir(III) complexes incorporating deprotonated 2-arylbenzimidazole ligands, **Ir1** and **Ir2**, and investigated their photophysical, cellular uptake and biological properties. A prepolymer was first designed and synthesized to facilitate the nanoencapsulation of the desired hydrophobic compounds without needing surfactants and under mild conditions given its self-emulsifying nature. This prepolymer incorporates suitable functional groups that dictate the pH-dependent amphoteric properties of the polymeric shell of the nanocapsules, as well as disulphide bonds to confer them degradability under reductive conditions. Both Ir(III) complex-loaded nanocapsules (**NC-Ir1** and **NC-Ir2**) showed a controlled particle size distribution of approximately 18 nm and a roughly round shape according to TEM micrographs, and high drug loading content, as determined by ICP-MS. The UV/Vis absorption and emission spectra of aqueous solutions of NCs were similar to those of the free complexes in CH_2Cl_2, which accounts for the hydrophobic environment generated by the nanoparticles around the cargo. The fact that the oxygen quenching of the emission was less efficient when the complexes were encapsulated also supports the protective effect provided by the nanocapsules.

Very importantly, we demonstrated by ICP-MS experiments that nanoencapsulation had a positive effect on the cellular uptake of the complexes since Ir accumulation from **NC-Ir1** and **NC-Ir2** after 2 h incubation in HeLa cells was 6 to 14– fold higher than those treated with the free complexes **Ir1** and **Ir2**, respectively, and that energy-dependent mechanisms were involved in the cellular uptake of the NCs. The Ir(III)-loaded nanocapsules **NC-Ir1** and **NC-Ir2** were found highly cytotoxic against cancer cells, including cisplatin sensitive and resistant ovarian cancer cells. By contrast, the free complexes **Ir1** and **Ir2** were found to be inactive against cells up to 100 µM which is in good agreement with their poor intracellular uptake. Importantly, cells treated with non-loaded NCs did not show antiproliferative activity and an absence of cytotoxicity was also observed in normal dividing cells (BGM), which indicates that Ir(III)-loaded agents may exhibit a preference for cancer cells. Besides showing high antiproliferative activities in 2D monolayer cancer cells, a strong tumor growth inhibition effect was also found in 3D tumorsphere cancer models after treatment with **NC-**

Ir1 and **NC-Ir2**, which can be attributed to the high penetration capacity of the small NCs. Finally, we explored the mode of cell death induced by these agents and found that oncosis or oncotic necrosis matched with the array of phenomena observed. Shortly after treatment, *i.e.* ~12 h, **NC-Ir1** and **NC-Ir2** produced cell swelling, blebbing and disruption of membrane permeability, which are features of oncotic cell death. Together with the plasma membrane leakage, mitochondrial dysfunction induced after 24 h and the generation of extensive oxidative stress appeared to be also involved in the mechanism of action of these Ir(III)-loaded nanoparticles.

SUPPLEMENTARY INFORMATION

Electronic supplementary information (ESI) available: General methods and analytical techniques. Additional figures for the synthesis and characterization of Ir(III) complexes (NMR, MS) and of the corresponding Ir(III)-loaded nanocapsules (IR, DLS, TEM, Z-potential, ICP-MS), and for their biological evaluation (confocal microscopy, antiproliferative activity, morphological analysis of cells, cell membrane integrity test, mitochondrial potential assessment, aerobic respiration and glycolytic rate evaluation and oxidative stress induction).

AUTHOR CONTRIBUTIONS

J.B., E.O.-F., G.V., M.B., N.C., J.R., J.R. and V.M. conceived the study. J.B. synthesized and characterized nanocapsules. G.V. synthesized and characterized Ir(III) complexes and performed photophysical studies. J.B. and M.B. performed confocal microscopy studies. E.O.-F. designed and performed all biological experiments. J.B., E.O.-F., G.V. and V.M. wrote the manuscript, which was contributed by all authors, who have approved the submitted version of the manuscript.

CONFLICTS OF INTEREST

There are no conflicts to declare.

ACKNOWLEDGEMENTS

REFERENCES

[1] S. Ghosh, Cisplatin: The first metal based anticancer drug, *Bioorg. Chem.*, 2019, **88**, 102925.

[2] a) D. M. Cheff and M. D. Hall, A Drug of Such Damned Nature. Challenges and Opportunities in Translational Platinum Drug Research, *J. Med. Chem.*, 2017, **60**, 4517–4532. b) R. Oun, Y. E. Moussa and N. J. Wheate, The side effects of platinum-based chemotherapy drugs: a review for chemists, *Dalton Trans.*, 2018, **47**, 6645-6653. c) T. C. Johnstone, K. Suntharalingam and S. J. Lippard, The Next Generation of Platinum Drugs: Targeted Pt(II) Agents, Nanoparticle Delivery, and Pt(IV) Prodrugs, *Chem Rev.*, 2016, **116**, 3436–3486.

[3] a) N. P. Barry and P.J. Sadler, Challenges for Metals in Medicine: How Nanotechnology May Help To Shape the Future, *ACS Nano*, 2013, **7**, 5654-5659. b) T. C. Johnstone, K. Suntharalingam and S. J. Lippard, The Next Generation of Platinum Drugs: Targeted Pt(II) Agents, Nanoparticle Delivery, and Pt(IV) Prodrugs, *Chem Rev.*, 2016, **116**, 3436–3486. c) X. Wang, X. Wang, S. Jin, N Muhammad and Z. Guo, Stimuli-Responsive Therapeutic Metallodrugs, *Chem. Rev.*, 2019, **119**, 1138−1192.

[4] a) L. Zeng, P. Gupta, Y. Chen, E. Wang, L. Ji, H. Chao and Z.-S. Chen, The development of anticancer ruthenium(II) complexes: from single molecule compounds to nanomaterials, *Chem. Soc. Rev.*, 2017, **46**, 5771-5804. b) M. Poursharifi, M. T. Wlodarczyk and A. J. Mieszawska, Nano-Based Systems and Biomacromolecules as Carriers for Metallodrugs in Anticancer Therapy, *Inorganics*, 2019, **7**, 2. c) P. Farinha, J. O Pinho, M. Matias and M. M. Gaspar, Nanomedicines in the treatment of colon cancer: a focus on metallodrugs, *Drug Deliv. Transl. Res.*, 2022, **12**, 49-66. d) M. He, F. Chen, D. Shao, P. Weis, Z. Wei and W. Sun, Photoresponsive metallopolymer nanoparticles for cancer theranostics, Biomaterials, 2021, **275**, 120915.

[5] Y. Zhang, H. Fu, S. Chen, B. Liu, W. Sun and H. Gao, Construction of an iridium(III)-complex-loaded MOF nanoplatform mediated with a dual-responsive polycationic polymer for photodynamic therapy and cell imaging, *Chem. Commun.*, 2020, **56**, 762-765.

[6] F. Ledezma-Gallegos, R. Jurado, R. Mir, L. A. Medina, L. Mondragon-Fuentes and P. García-López, Liposomes Co-Encapsulating Cisplatin/Mifepristone Improve the Effect on Cervical Cancer: In Vitro and In Vivo Assessment, *Pharmaceutics*, 2020, **12**, 897.

[7] H. Xiang, H. Chen, H. P. Tham, S. Z. F. Phua, J.-G. Liu and Y. Zhao, Cyclometalated Iridium(III)-Complex-Based Micelles for Glutathione-Responsive Targeted Chemotherapy and Photodynamic Therapy, *ACS Appl. Mater. Interfaces*, 2017, **9**, 27553−27562.

[8] S. Dhar, N. Kolishetti, S. J. Lippard and O. C. Farokhzad, Targeted delivery of a cisplatin prodrug for safer and more effective prostate cancer therapy in vivo, *Proc. Nat. Acad. Sci. U.S.A.*, 2011, **108**, 1850-1855.

[9] J. Karges, J. Li, L. Zeng, H. Chao and G. Gasser, Polymeric Encapsulation of a Ruthenium Polypyridine Complex for Tumor Targeted One- and Two-Photon Photodynamic Therapy, *ACS Appl. Mater. Interfaces*, 2020, **12**, 54433−54444.

[10] N. Gadzhiev, D. Gorelov, V. Malkhasyan, G. Akopyan, R. Harchelava, D. Mazurenko, C Kosmala, Z. Okhunov and S. Petrov, Comparison of silicone versus polyurethane ureteral stents: a prospective controlled study, *BMC Urology*, 2020, **20**, 10.

[11] Y. Liu,| Y. Zou, J. Wang, S. Wang and X. Liu, A novel cationic waterborne polyurethane coating modified by chitosan biguanide hydrochloride with application potential in medical catheters, *J. Appl. Polym. Sci.*, 2021, **138**, e50290.

[12] L. Zhou, D. Liang, X. He, J. Li, H. Tan, J. Li, Q Fu and Q Gu, The degradation and biocompatibility of pH-sensitive biodegradable polyurethanes for intracellular multifunctional antitumor drug delivery, *Biomaterials*, 2012, **33**, 2734-2745.

[13] A. Schoth, K. Landfester and R. Muñoz-Espí, Surfactant-Free Polyurethane Nanocapsules via Inverse Pickering Miniemulsion, *Langmuir*, 2015, **31**, 3784−3788.

[14] P. Rocas, C. Cusco, J. Rocas and F. Albericio, On the Importance of Polyurethane and Polyurea Nanosystems for Future Drug Delivery, *Curr. Drug Delivery*, 2018, **15**, 37-43.

[15] G. Flórez-Graua, P. Rocas, R. Cabezón, C España, J Panés, J. Rocas, F. Albericio and D Benítez-Ribas, Nanoencapsulated budesonide in self-stratified polyurethane-polyurea nanoparticles is highly effective in inducing human tolerogenic dendritic cells, *Int. J. Pharm.*, 2016, **511**, 785-793.

[16] P. Rocas, M. Hoyos-Nogués, J. Rocas, J. M. Manero, J. Gil, F. Albericio and C. Mas-Moruno, Installing Multifunctionality on Titanium with RGD Decorated Polyurethane-

Polyurea Roxithromycin Loaded Nanoparticles: Toward New Osseointegrative Therapies, *Adv. Healthcare Mater.*, 2015, **4**, 1956–1960.

[17] C. Cuscó, J. Garcia, E. Nicolás, P. Rocas and J. Rocas, Multisensitive drug-loaded polyurethane/polyurea nanocapsules with pH-synchronized shell cationization and redox-triggered release, *Polym. Chem.*, 2016, **7**, 6457-6466.

[18] a) A. Zamora, G. Vigueras, V. Rodríguez, M. D. Santana and J. Ruiz, Cyclometalated iridium(III) luminescent complexes in therapy and phototherapy, *Coord, Chem. Rev.*, 2018, **360**, 34–76. b) D.-L. Ma, D. S.-H. Chan and C.-H. Leung, Group 9 Organometallic Compounds for Therapeutic and Bioanalytical Applications, *Acc. Chem. Res.*, 2014, **47**, 3614–3631.

[19] a) P.-Y. Ho, C.-L. Ho and W.-Y. Wong, Recent advances of iridium(III) metallophosphors for health-related applications, *Coord. Chem. Rev.,* 2020, **413**, 213267. b) C.-P. Tan, Y.-M. Zhong, L.-N. Jia and Z.-W. Mao, Phosphorescent metal complexes as theranostic anticancer agents: combining imaging and therapy in a single molecule, *Chem. Sci.*, 2021, **12**, 2357-2367.

[20] a) A. R. Bin Mohd Yusoff, A. J. Huckaba and M. K. Nazeeruddin, Phosphorescent Neutral Iridium (III) Complexes for Organic Light-Emitting Diodes, *Top. Curr. Chem. (Z)*, 2017, **375**, 39. b) E. Longhia and L. De Cola, Iridium(III) Complexes for OLED Application. In Iridium(III) in Optoelectronic and Photonics Applications; John Wiley & Sons, Ltd, 2017; pp 205–274.

[21] a) K. Yokoi, Y. Hisamatsu, K. Naito and S. Aoki, Design, Synthesis, and Anticancer Activities of Cyclometalated Tris(2-phenylpyridine)iridium(III) Complexes with Cationic Peptides at the 4′-Position of the 2-Phenylpyridine Ligand, *Eur. J. Inorg. Chem.*, 2017, **44**, 5295–5309. b) K. Yokoi, C. Balachandran, M. Umezawa, K. Tsuchiya, A. Mitrić and S. Aoki, Amphiphilic Cationic Triscyclometalated Iridium(III) Complex–Peptide Hybrids Induce Paraptosis-like Cell Death of Cancer Cells via an Intracellular Ca^{2+}-Dependent Pathway, *ACS Omega*, 2020, **5**, 6983–7001.

[22] a) K. Qiu, H. Huang, B. Liu, Y. Liu, Z. Huang, Y. Chen, L. Ji and H. Chao, Long-Term Lysosomes Tracking with a Water-Soluble Two-Photon Phosphorescent Iridium(III) Complex, *ACS Appl. Mater. Interfaces*, 2016, **8**, 12702–12710. b) B. Liu, S. Monro, M. A. Jabed, C. G. Cameron, K. L. Colón, W. Xu, S. Kilina, S. A. McFarland and W. Sun, Neutral iridium(iii) complexes bearing BODIPY-substituted N-heterocyclic carbene (NHC) ligands:

synthesis, photophysics, in vitro theranostic photodynamic therapy, and antimicrobial activity, *Photochem. Photobiol. Sci.*, 2019, **18**, 2381-2396.

[23] a) A. Sansee, S. Meksawangwong, K. Chainok, K. J. Franz, M. Gál, L.-O. Pålsson, W. Puniyan, R. Traiphol, R. Pal and F. Kielar, Novel aminoalkyl tris-cyclometalated iridium complexes as cellular stains, *Dalton Trans.*, 2016, **45**, 17420–17430. b) A. Nakagawa, Y. Hisamatsu, S. Moromizato, M. Kohno and S. Aoki, Synthesis and Photochemical Properties of pH Responsive Tris-Cyclometalated Iridium(III) Complexes That Contain a Pyridine Ring on the 2-Phenylpyridine Ligand, Inorg. Chem., 2014, **53**, 409–422.

[24] Z. Feng, P. Tao, L. Zou, P. Gao, Y. Liu, X. Liu, H. Wang, S. Liu, Q. Dong, J. Li, B. Xu, W. Huang, W.-Y. Wong and Q. Zhao, Hyperbranched Phosphorescent Conjugated Polymer Dots with Iridium(III) Complex as the Core for Hypoxia Imaging and Photodynamic Therapy, *ACS Appl. Mater. Interfaces*, 2017, **9**, 28319–28330.

[25] a) Y. Fan, C. Li, F. Li and D. Chen, pH-activated size reduction of large compound nanoparticles for in vivo nucleus-targeted drug delivery, *Biomaterials*, 2016, **85**, 30-39. b) S. C. Larnaudie, J. C. Brendel, I. Romero-Canelón, C. Sanchez-Cano, S. Catrouillet, J. Sanchis, J. P. C. Coverdale, J.-I. Song, A. Habtemariam, P. J. Sadler, K. A. Jolliffe and S. Perrier, Cyclic Peptide−Polymer Nanotubes as Efficient and Highly Potent Drug Delivery Systems for Organometallic Anticancer Complexes, *Biomacromolecules*, 2018, **19**, 239−247. c) C. Liao, D. Xu, X. Liu, Y. Fang, J. Yi, X. Li and B. Guo, Iridium (III) complex-loaded liposomes as a drug delivery system for lung cancer through mitochondrial dysfunction, *Int. J. Nanomed.*, 2018, **13**, 4417–4431. d) W.-Y. Zhang, F. Du, M. He, L. Bai, Y.-Y. Gu, L.-L. Yang and Y.-J. Liu, Studies of anticancer activity in vitro and in vivo of iridium(III) polypyridyl complexes-loaded liposomes as drug delivery system, *Eur. J. Med. Chem.*, 2019, **178**, 390-400.

[26] a) P. Singla, V. Luxami and K. Paul, Benzimidazole-biologically attractive scaffold for protein kinase inhibitors, *RSC Adv.*, 2014, **4**, 12422–12440. b) Y. Bansal and O. Silakari, The therapeutic journey of benzimidazoles: a review, *Bioorg. Med. Chem.*, 2012, **20**, 6208–6236.

[27] a) J. Pracharova, G. Vigueras, V. Novohradsky, N. Cutillas, C. Janiak, H. Kostrhunova, J. Kasparkova, J. Ruiz and V. Brabec, Exploring the Effect of Polypyridyl Ligands on the Anticancer Activity of Phosphorescent Iridium(III) Complexes: From Proteosynthesis Inhibitors to Photodynamic Therapy Agents, *Chem. Eur. J.*, 2018, **24**, 4607–4619. b) V. Novohradsky, G. Vigueras, J. Pracharova, N. Cutillas, C. Janiak, H. Kostrhunova, V. Brabec, J. Ruiz and J. Kasparkova, Molecular superoxide radical photogeneration in cancer cells by

dipyridophenazine iridium(iii) complexes, *Inorg. Chem. Front.*, 2019, **6**, 2500–2513. c) V. Novohradsky, A. Rovira, C. Hally, A. Galindo, G. Vigueras, A. Gandioso, M. Svitelova, R. Bresolí-Obach, H. Kostrhunova, L. Markova, J. Kasparkova, S, Nonell, J. Ruiz, V. Brabec and V. Marchán, Towards Novel Photodynamic Anticancer Agents Generating Superoxide Anion Radicals: A Cyclometalated Ir[III] Complex Conjugated to a Far-Red Emitting Coumarin, *Angew. Chem. Int. Ed.*, 2019, **58**, 6311–6315. d) V. Novohradsky, L. Markova, H. Kostrhunova, J. Kasparkova, J. Ruiz, V. Marchán and V. Brabec, A Cyclometalated IrIII Complex Conjugated to a Coumarin Derivative Is a Potent Photodynamic Agent against Prostate Differentiated and Tumorigenic Cancer Stem Cells, *Chem. Eur. J.*, 2021, **27**, 8547-8556.

[28] J. Yellol, S. A. Pérez, G. Yellol, J. Zajac, A. Donaire, G. Vigueras, V. Novohradsky, C. Janiak, V. Brabec and J. Ruiz, Highly potent extranuclear-targeted luminescent iridium(III) antitumor agents containing benzimidazole-based ligands with a handle for functionalization, *Chem. Commun.*, 2016, **52**, 14165–14168.

[29] M. C. DeRosa, D. J. Hodgson, G. D. Enright, B. Dawson, C. E. B. Evans and R. J. Crutchley, Iridium Luminophore Complexes for Unimolecular Oxygen Sensors, *J. Am. Chem. Soc.*, 2004, **126**, 7619–7626.

[30] H. J. Lee and Y. Ha, Heteroleptic Orange Light-Emitting Iridium Complexes Containing Phenylbenzothiazolate Ligands, *Polym. Bull.*, 2016, **73**, 2501–2509.

[31] T.R. Chen, Microscopic demonstration of mycoplasma contamination in cell cultures and cell culture media, *Tca Manual*, 1975, **1**, 229–232.

[32] J. Schindelin, I. Arganda-Carreras, E. Frise, V. Kaynig, M. Longair, T. Pietzsch, S. Preibisch, C. Rueden, S. Saalfeld, B. Schmid, J.-Y- Tinevez, D. J. White, V. Hartenstein, K. Eliceiri, P. Tomancak and A. Cardona, Fiji: An Open-Source Platform for Biological-Image Analysis, *Nat. Methods*, 2012, **9**, 676–682.

[33] K. Dedeian, J. Shi, N. Shepherd, E. Forsythe and D. C. Morton, Photophysical and Electrochemical Properties of Heteroleptic Tris-Cyclometalated Iridium(III) Complexes, *Inorg. Chem.*, 2005, **44**, 4445–4447.

[34] A. Tsuboyama, H. Iwawaki, M. Furugori, T. Mukaide, J. Kamatani, S. Igawa, T. Moriyama, S. Miura, T. Takiguchi, S. Okada, M. Hoshino and K. Ueno, Homoleptic Cyclometalated Iridium Complexes with Highly Efficient Red Phosphorescence and Application to Organic Light-Emitting Diode, *J. Am. Chem. Soc.*, 2003, **125**, 12971–12979.

[35] Z. Li, Synthesis, Photophysics, and Reverse Saturable Absorption of 7-(Benzothiazol-2-Yl)-9,9-Di(2-Ethylhexyl)-9H-Fluoren-2-Yl Tethered [Ir(Bpy)(Ppy)$_2$]PF$_6$ and Ir(Ppy)$_3$ Complexes (Bpy = 2,2′-Bipyridine, Ppy = 2-Phenylpyridine), *RSC Adv.*, 2016, **6**, 41214–41228.

[36] M. Pérez-Hernández, C. Cuscó, C. Benítez-García, J. Bonelli, M. Nuevo-Fonoll, A-Soriano, D. Martínez-García, A. Arias-Betancur, M. García-Valverde, M. F. Segura, R. Quesada, J. Rocas, V. Soto-Cerrato and R. Pérez-Tomás, Multi-Smart and Scalable Bioligands-Free Nanomedical Platform for Intratumorally Targeted Tambjamine Delivery, a Difficult to Administrate Highly Cytotoxic Drug, *Biomedicines*, 2021, **9**, 508.

[37] a) A. L. Tessaro, A: Fraix, M. Failla, V. Cardile, A. C. E. Graziano, B. M. Estevao, A. Rescifina and S. Sortino, Light-controlled simultaneous "on demand" released of cytotoxic combinations for bimodal killing of cancer cells, *Chem. Eur. J*., 2018, **24**, 7664-7670. b) A. Wicki, D. Witzigmann, V. Balasubramanian and J. Huwyler, Nanomedicine in cancer therapy: challenges, opportunities, and clinical applications, *J. Controlled Release*, 2015, **200**, 138-157.

[38] V. P. Chauhan, T. Stylianopoulos, J. D. Martin, Z. Popović, O. Chen, W. S. Kamoun, M.G. Bawendi, D. Fukumura and R. K. Jain, Normalization of tumour blood vessels improves the delivery of nanomedicines in a size-dependent manner, *Nature Nanotech.*, 2012, **7**, 383–388.

[39] a) F. Danhier, O. Feron and V. Préa, To exploit the tumor microenvironment: Passive and active tumor targeting of nanocarriers for anti-cancer drug delivery, J. *Controlled Release*, 2010, **148**, 135–146. b) M. Wang, A. D. Miller and M. Thanou, *J. Drug Targeting*, 2013, **21**, 684-692. c) A. Verma and F. Stellacci. *Small*, 2010, **6**, 12-21.

[40] A. Latorre and A. Somoza, Glutathione-Triggered Drug Release from Nanostructures, *Curr. Top. Med. Chem.*, 2014, **14**, 2662-2671.

[41] A. Bansal and M. Celeste Simon, Glutathione metabolism in cancer progression and treatment resistance, *J. Cell Biol.*, 2018, **217**, 2291-298.

[42] a) J. Carretero, E. Obrador, M. J. Anasagasti, J. J. Martin, F. Vidal-Vanaclocha and J. M. Estrela, Growth-associated changes in glutathione content correlate with liver metastatic activity of B16 melanoma cells, *Clin. Exp. Metastasis*, 1999, **17**, 567. b) D. Yoo, E. Jung, J. Noh, H. Hyun, S. Seon, S. Hong, D. Kim and D. Lee, Glutathione-Depleting Pro-Oxidant as a Selective Anticancer Therapeutic Agent, *ACS Omega*, 2019, **4**, 10070-10077.

[43] a) P. Laskar, S. Somani, S. J. Campbell, M. Mullin, P. Keating, R. J. Tate, C. Irving, H. Y. Leung and C. Dufès, Camptothecin-based dendrimersomes for gene delivery and redox-responsive drug delivery to cancer cells, *Nanoscale*, 2019, **11**, 20058-20071. b) X. Jia, J. He, L. Shen, J. Chen, Z. Wei, X. Qin, D. Niu, Y. Li and J. Shi, Gradient Redox-Responsive and Two-Stage Rocket-Mimetic Drug Delivery System for Improved Tumor Accumulation and Safe Chemotherapy, *Nano Letters*, 2019, **19**, 8690-8700. c) Y. Nie, Y. Xu, Y. Gao, J. He, L. Sun, J. Chen, Y. Cui, H. Ge and X. Ning, A glutathione-triggered precision explosive system for improving tumor chemosensitivity, *Nano Res.*, 2021, **14**, 2372-2382.

[44] L. Kennedy, J. K. Sandhu, M. E. Harper and M. Cuperlovic-Culf, Role of Glutathione in Cancer: From Mechanisms to Therapies, *Biomolecules*, 2020, **10**, 1429.

[45] a) Q. Mei, R. Sheng, W. Cheng, J. Zhang, P. Wang, Q. Mei, P. Chen and B. Tong, High stability and luminance efficiency thieno[2,3-d]pyridazine-based iridium complexes and their applications in high-performance yellow OLEDs, *Dalton Trans.*, 2020, **49**, 13797–13804. b) S. Meksawangwong, B. Gohil, W. Punyain, R. Pal and F. Kielar, Development of tris-cyclometalated iridium complexes for cellular imaging through structural modification, *Inorg. Chim. Acta*, 2020, **508**, 119609. c) T. Giridhar, J.-H. Lee, W. Cho, H. Yoo, C.-K. Moon, J.-J. Kim and S.-H. Jin, Highly efficient bluish green phosphorescent organic light-emitting diodes based on heteroleptic iridium(III) complexes with phenylpyridine main skeleton, *Org. Electron.*, 2014, **15**, 1687–1694. d) J. C. Deaton, R. H. Young, J. R. Lenhard, M. Rajeswaran and S. Hu., Photophysical Properties of the Series fac- and mer-(1-Phenylisoquinolinato-N∧C2′)x(2-phenylpyridinato-N∧C2′)3−xIridium(III) (x= 1−3), *Inorg. Chem.*, 2010, **49**, 9151–9161.

[46] H. Lu and M. H Stenzel, Multicellular Tumor Spheroids (MCTS) as a 3D In Vitro Evaluation Tool of Nanoparticles, *Small*, 2018, **14**, 1702858

[47] S. Sperandio, I. de Belle and D. E. Bredesen, An alternative, nonapoptotic form of programmed cell death, *Proc. Natl. Acad. Sci. U. S. A.*, 2000, **97**, 14376–14381.

[48] P. Weerasinghe and L. M. Buja, Oncosis: an important non-apoptotic mode of cell death, *Exp. Mol. Pathol.*, 2012, **93**, 302-308.

[49] a) R. S. Whelan, K. Konstantinidis, A.-C. Wei, Y. Chen, D. E. Reyna, S. Jha, Y. Yang, J. W. Calvert, T. Lindsten, C. B. Thompson, M. T. Crow, E. Gavathiotis, G. W. Dorn II, B. O'Rourke and R. N. Kitsis, Bax regulates primary necrosis through mitochondrial dynamics,

Proc. Natl. Acad. Sci. U.S.A., 2012, **109**, 6566-6571. b) P. Golstein and G. Kroemer, Cell death by necrosis: towards a molecular definition, *Trends Biochem. Sci*., 2007, **32**, 37-43.

[50] M. G Vander Heiden, L. C Cantley and C. B Thompson, Understanding the Warburg effect: the metabolic requirements of cell proliferation, *Science*, 2009, **324**, 1029-1033.

[51] S. W. Ryter, H. P. Kim, A. Hoetzel, J. W. Park, K. Nakahira, X. Wang and A. M. K. Cho, Mechanisms of Cell Death in Oxidative Stress, *Antioxid. Redox Signal.*, 2007, **9**, 49-89.